Electrooxidation of methanol on highly active and stable Pt–Sn–Ce/C catalyst for direct methanol fuel cells

Arun Murthy, Eungje Lee, Arumugam Manthiram*

Electrochemical Energy Laboratory & Materials Science and Engineering Program, University of Texas at Austin, Austin, TX 78712, United States

ABSTRACT

Carbon supported Pt–Sn–Ce and Pt–Sn catalysts have been synthesized by a polyol reduction method and compared for methanol oxidation reaction (MOR). X-ray photoelectron spectroscopic (XPS), X-ray diffraction (XRD), and transmission electron microscopic (TEM) analyses reveal the beneficial effects of the Ce component in Pt–Sn–Ce/C for MOR, despite its low content. Electrochemical techniques such as CO_{ad} stripping, linear scan, and derivative voltammetries along with electrochemical impedance spectroscopy (EIS) were employed to analyze MOR on Pt–Sn–Ce/C and Pt–Sn/C from a mechanistic point of view. Accelerated durability test (ADT) and single cell test of Pt–Sn–Ce/C in comparison to a commercial PtRu/C catalyst demonstrate the superior performance of Pt–Sn–Ce/C from stability and activity points of view.

© 2012 Elsevier B.V. All rights reserved.

1. Introduction

Among the low temperature fuel cells, direct methanol fuel cells (DMFC) offer several advantages over especially the polymer electrolyte membrane fuel cells (PEMFC) employing hydrogen as a fuel. Methanol is a liquid fuel and the infrastructure for handling, transportation, and distribution of a liquid fuel is already established. Moreover, methanol is cheaper and has high theoretical energy density [1]. On the downside, despite being a simple one-carbon alcohol, the methanol oxidation reaction (MOR) is complicated, producing several intermediates such as formaldehyde and formic acid and poisonous species such as carbon monoxide that lead to low efficiency [2,3]. Platinum-based catalysts have been widely investigated for MOR with a secondary metal assisting the complete oxidation of methanol to CO_2 through electronic effect, bifunctional mechanism, and geometric effect [4–7]. Pt–Ru is a well-known electrocatalyst having the highest activity toward MOR among the known binary catalysts [8–10]. However, in recent times, there have been several efforts to identify an alternative anode catalyst to replace Pt–Ru mainly because (i) Pt–Ru does not retain its initial activity for long-term applications due to Ru dissolution and (ii) the Ru component is nearly as expensive as Pt [11,12]. Pt–Sn is another well-studied catalyst for MOR and its activity is comparable to that of Pt–Ru [13–16]. The catalytic activity of Pt–Sn varies largely depending on the method of synthesis, degree of alloying of Sn, oxidation state of Sn, and Sn content in the catalyst.

In a recent study, we synthesized Pt–Ru/C and Pt–Sn/C catalysts by a polyol reduction method and compared their stability in different potential domains [17]. Even though the initial activity of Pt–Sn/C was lower than that of Pt–Ru/C, it showed very high electrochemical stability with a negligible dissolution of Sn as confirmed by inductively coupled plasma-optical emission spectroscopy (ICP-OES) at the end of accelerated durability test (ADT) [17]. In an effort to enhance the MOR activity, we embarked on adding a third non-ruthenium component to the binary Pt–Sn catalyst. For example, the addition of cerium in its oxide form could enhance the activity of Pt–Sn. It is well known that Ce can exist in a mixed $3^+/4^+$ oxidation state in its oxide $CeO_{2-\delta}$, which could reversibly incorporate oxygen and thereby enhance the oxidative removal of the poisonous intermediates formed during MOR. In a recent study [18], the effect of addition of various metal oxides to Pt was evaluated using electrochemical impedance spectroscopy (EIS), wherein platinum–cerium oxide showed higher MOR activity compared to that of platinum–tin oxide. We present in this paper the synthesis of carbon-supported Pt–Sn and Pt–Sn–Ce catalysts and compare their physical and electrochemical characteristics. The MOR activity and electrochemical stability of Pt–Sn–Ce/C are evaluated and compared with those of a commercial PtRu/C catalyst, employing voltammetric and single cell methods. The superior performance of Pt–Sn–Ce/C is attributed to the beneficial effects of the Ce component on the alloying of Sn, particle size, and oxidation of CO_{ad} through a synergetic mechanism.

* Corresponding author. Tel.: +1 512 471 1791; fax: +1 512 471 7681.
  E-mail address: rmanth@mail.utexas.edu (A. Manthiram).

2. Experimental

Carbon-supported Pt–Sn, and Pt–Sn–Ce catalysts were prepared with a 40 wt.% metal loading by a polyol method employing $H_2PtCl_6·6H_2O$ (Strem Chemicals Inc.), $SnCl_2·2H_2O$ (Acros Organics), and $Ce(NO_3)_3·6H_2O$ (Aldrich) as metal sources and ethylene glycol (Fisher Scientific) as the solvent and reducing agent. In a typical procedure, the required quantities of $H_2PtCl_6·6H_2O$, $SnCl_2·2H_2O$, and $Ce(NO_3)_3·6H_2O$ (in the case of Pt–Sn–Ce) were dissolved in 120 mL of ethylene glycol containing 0.1 M NaOH (Fisher Chemical) to obtain 60 mg of total metal weight. The solution was refluxed at 160 °C for 3 h under open atmosphere until the color of the solution changed to dark brown, indicating the formation of a colloid of metal nanoparticles. 90 mg of carbon black (Vulcan XC-72R) was dispersed separately in 200 mL of ethylene glycol/water (1:1 ratio by volume) by ultrasonication. The metal colloid was then added slowly to the carbon dispersion under stirring, and subsequently a few drops of aqueous 2 M H_2SO_4 were added until the pH of the mixture reached 2. The resulting dispersion was stirred vigorously for 6 h to facilitate the deposition of the colloidal nanoparticles onto the carbon surface. After cooling to room temperature, the mixture was filtered and washed with copious amount of water. Finally, the residue was dried overnight in a vacuum oven at 90 °C.

XRD data were collected with a powder diffractometer (XRD, Philips) in the range of 20–80° with a step of 0.03°. The lattice parameter values were obtained by fitting the (2 2 0) reflections using the pseudo-Voigt function. The powder diffractometer was previously calibrated and the peak fitting was carried out without considering zero angle shifts and sample displacements. Transmission electron microscopy (TEM) data were collected with a JEOL 2010F equipment to characterize the morphology and crystallite size, d_{TEM}, of the catalyst nano particles. The size distribution of the nanoparticles was obtained by examining more than 100 particles in the TEM image. X-ray photoelectron spectroscopic (XPS) data were obtained with a Kratos Analytical XPS instrument using monochromatic Al Kα X-ray source to assess the surface oxidation states and quantify Pt, Sn, and Ce in the catalysts. The spectra were fitted with a Gaussian–Lorentzian function (G:L = 70:30) and a Shirley/linear background function using the CASAXPS software. The surface compositions of the catalysts were obtained by energy dispersive spectroscopy (EDS, Oxford instruments) attached to a scanning electron microscope (SEM, JEOL-JSM5610).

Voltammetric experiments were conducted with a CH Instruments potentiostat in a conventional single compartment three-electrode cell having a platinum wire counter electrode and a Hg/HgSO4 reference electrode (in saturated K_2SO_4 solution). The potentials were, however, referenced with respect to the reversible hydrogen electrode (RHE) in this study. A glassy carbon (3 mm diameter) electrode was polished to a mirror-like finish with 0.05 μm alumina media (Buehler) and coated with a thin layer of the catalyst to serve as a working electrode. The catalyst ink was prepared by dispersing 2 mg of the catalyst in a mixture of deionized water, ethanol, and Nafion (Electrochem Inc., obtained as 5 wt.% solution) through ultrasonic vibration. 2 μL of the resulting ink was drop cast onto the glassy carbon electrode and subsequently dried in air. During voltammetric experiments, the electrode potential was scanned between 0.02 and 1.2 V

initially for 10 cycles at a scan rate of 50 mV/s in 0.5 M H_2SO_4 to clean the catalyst surface. MOR activities of the catalysts were evaluated in a nitrogen saturated 0.5 M H_2SO_4 + 1 M methanol solution at a scan rate of 50 mV/s. The first derivative of linear sweep voltammogram was computed in Matlab by transferring the voltammetric data to the Matlab workspace. CO_{ad} stripping voltammetry was carried out by purging the electrolyte with high purity CO gas for 30 min at a holding potential of 0.1 V. The purging gas was then switched to nitrogen to remove dissolved CO. CO_{ad} was then stripped by scanning the potential between 0.05 and 1.2 V at a rate of 20 mV/s. Impedance analysis was carried out with a Solartron 1260 frequency response analyzer and Solartron 1286 potentiostat/galvanostat controlled by ZPLOT2 software from Scribner. The frequency range explored was from 100 mHz to 5 kHz with an amplitude of 5 mV.

The single cell performances of the Pt–Sn–Ce/C and PtRu/C (40 wt.% PtRu on carbon, ETEK Inc.) anodes were assessed in the cells with identical cathodes (Pt/C, 40 wt.%, ETEK, Inc) and membranes (Nafion 115). The anode/cathode catalyst ink was prepared by sonicating the required amounts of the catalyst and Nafion (25% the weight of the catalyst) in isopropyl alcohol (50 times the weight of the catalyst) + deionized water (30 times the weight of the catalyst) for 1 h. The catalyst ink was air sprayed onto a gas-diffusion layer (BASF), followed by drying in air at 90 °C. The catalyst loading was 3 mg/cm^2 for both the anode and the cathode. The membrane-electrode assemblies (MEA) were fabricated by hot pressing the anode and cathode onto a Nafion 115 membrane at 120 °C and 80 psi for 2.5 min. The single cell hardware (Scribner) with serpentine flow-field pattern (5 cm^2 active area) was used for feeding 1 M methanol solution (flow rate: 2.5 mL/min) and humidified oxygen (flow rate: 200 mL/min, 16 psi cathode backpressure) at 80 °C.

3. Results and discussion

3.1. Effect of addition of Ce on the electrocatalytic activity of Pt–Sn–Ce/C

The compositions of the as-prepared catalysts were obtained from XPS quantification analysis and EDS analysis (Table 1). The observed composition of Pt–Sn/C is 3:1, which is same as the nominal composition. However, the observed composition of Pt–Sn–Ce/C is 2.8:1:0.2, while the nominal composition based on metal precursors is 3:1:1. The loss of Ce can be attributed to adsorption processes wherein the colloids of metal/metal oxides were adsorbed on carbon support at a lower pH resulting in dissolution of ceria. In a recent study [19], a lower content of the third metal component in a ternary system Pt–Sn–Ru/C (1:1:0.3) showed higher activity for ethanol oxidation reaction (EOR) compared to the binary systems Pt–Sn/C (1:1) and Pt–Ru/C (1:1) as well as the ternary Pt–Sn–Ru/C (1:1:1) catalyst. Fig. 1 shows the XPS spectra of the Pt–Sn/C and Pt–Sn–Ce/C catalysts and Table 1 lists the assignments of the deconvoluted spectra to various oxidation states and their relative percentages. The Pt 4f XPS signals (Fig. 1a,d) consists of two peaks corresponding to the $4f_{5/2}$ and $4f_{7/2}$ states and each peak could be deconvoluted into three different Pt oxidation states of Pt(0), Pt(II), and Pt(IV). The predominant lowest binding energy peaks of Pt $4f_{7/2}$ (around 71 eV) and Pt $4f_{5/2}$ (around 74.5 eV)

Table 1
Binding energy (B.E.) values of Pt–Sn–Ce/C and Pt–Sn/C, with the relative % of different oxidation states indicated in parenthesis and the atomic ratios obtained from XPS and EDS analyses.

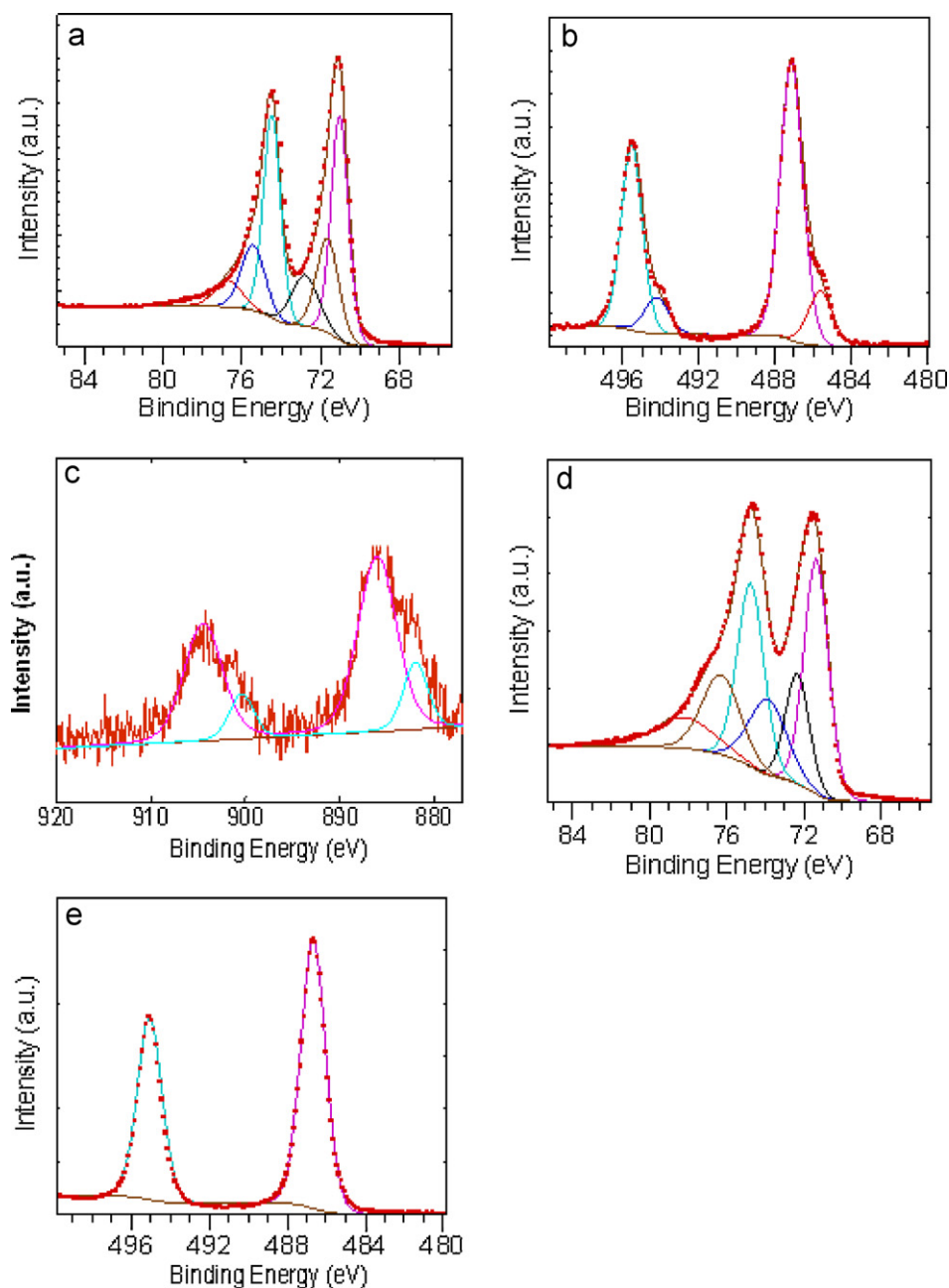| Catalyst	Binding energy (eV)							Atomic ratio	
	Pt(0) $4f_{7/2}$	Pt(II) $4f_{7/2}$	Pt(IV) $4f_{7/2}$	Sn(0) $3d_{5/2}$	Sn(IV) $3d_{5/2}$	Ce(III) 3d		XPS	EDS
Pt–Sn–Ce	71.19 (73)	71.83 (18)	73.33 (9)	485.49 (18)	487.11 (82)	882.1 (100)	901.1 (100)	2.8:1:0.2	2.8:1:0.12
Pt–Sn	71.41 (70)	72.63 (22)	74.13 (8)	–	486.69 (100)	–	–	3:1	3:1

Fig. 1. X-ray photoelectron spectra of (a) Pt 4f of Pt–Sn–Ce/C, (b) Sn 3d of Pt–Sn–Ce/C, (c) Ce 3d of Pt–Sn–Ce/C, (d) Pt 4f of Pt–Sn/C, and (e) Sn 3d of Pt–Sn/C.

states correspond to Pt(0). The peak around 72 eV (Pt $4f_{7/2}$) can be assigned to Pt(II) oxidation state due to PtO or Pt(OH)$_2$ species formed on the surface of Pt. The corresponding $4f_{5/2}$ peak for Pt(II) oxidation state appear around 76 eV. The smallest deconvoluted peaks of $4f_{7/2}$ and $4f_{5/2}$ states are ascribed to Pt(IV) due to species such as PtO$_2$. Comparing the binding energy values of the Pt 4f spectra of Pt–Sn/C and Pt–Sn–Ce/C, a shift to lower energies (0.2–0.6 eV) is seen in the Pt–Sn–Ce/C catalyst. This may be caused by the electro negativity difference between Pt and Ce. A charge transfer between less electronegative Ce and more electronegative Pt may be assumed [14]. The Sn 3d spectrum of Pt–Sn–Ce/C can be deconvoluted into two peaks while that of Pt–Sn/C has no contribution from second species (Fig. 1b,e). The lower binding energy peaks of Pt–Sn–Ce/C are due to Sn(0) while the higher binding energy peaks can be attributed to oxidized species such as Sn(II) or Sn(IV). Discriminating Sn(II) from Sn(IV) is difficult owing to a small difference

between the binding energies [14]. In the case of Pt–Sn/C, inferring from the peak position, the Sn 3d spectrum can be assigned to oxidized species like Sn(II) or Sn(IV). Fig. 1c shows the Ce 3d spectrum of Pt–Sn–Ce/C, which is commonly used to study ceria. Six 3d peaks are expected for CeO$_2$ and four for Ce$_2$O$_3$ [20]. Only four deconvoluted peaks are observed in Fig. 1c. Furthermore, a peak around 915 eV unique to CeO$_2$ is absent in the spectrum; hence Ce$_2$O$_3$ may be the predominant species present in Pt–Sn–Ce/C.

Fig. 2 shows the diffractograms of Pt–Sn/C and Pt–Sn–Ce/C catalysts along with that of 40 wt.% commercial Pt/C (ETEK) for a comparison. Crystalline face centered cubic (fcc) phases with characteristic peaks from (1 1 1), (2 0 0), (2 2 0), and (3 1 1) planes form a prominent pattern in all the diffractograms. Compared to the Pt/C pattern, the peaks are broader in Pt–Sn/C and Pt–Sn–Ce/C catalysts indicating a smaller particle size effect. Furthermore, weak reflections (marked with circles) observed at around 34° and 52°
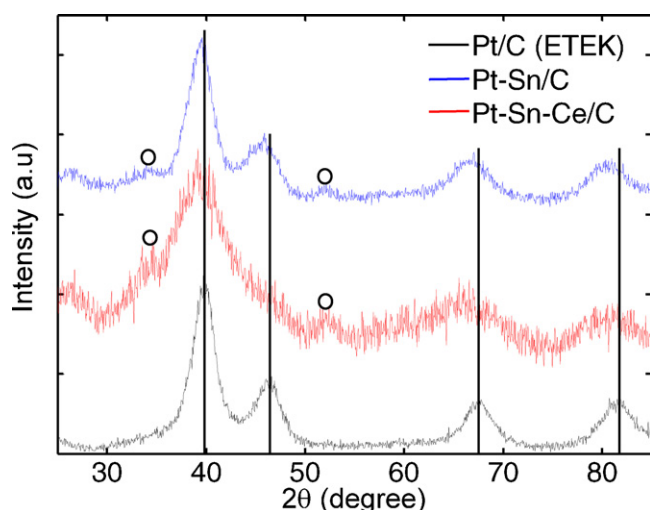
Fig. 2. X-ray diffraction patterns of Pt/C (ETEK), Pt–Sn/C, and Pt–Sn–Ce/C. The solid lines indicate the diffraction angles of typical Pt fcc phase. The circles represent the positions of SnO$_2$ tetragonal phase.

are attributed to (1 0 1) and (2 1 1) reflections of tetragonal SnO$_2$ phase and no peaks corresponding to cubic Pt$_3$Sn or hexagonal PtSn phases are observed [21]. The diffraction peaks of Pt–Sn/C and Pt–Sn–Ce/C are slightly shifted toward lower 2θ values compared to those of Pt/C, suggesting an alloying of Sn with Pt. Incorporation of relatively larger Sn atoms (0.151 nm) into the fcc structure of Pt (0.139 nm) results in an increase in lattice parameter (a_{fcc}) as seen in Table 2. The particle sizes (d_{XRD}) of the Pt–Sn and Pt–Sn–Ce samples were calculated from the XRD data using full width at half maximum (FWHM) and the angular position of Gaussian-fitted (2 2 0) peaks according to the Scherrer equation (Table 2) [22,23]. Pt–Sn–Ce has smaller d_{XRD} than Pt–Sn/C. The Sn atomic fraction (X_{Sn}) in the Pt–Sn/C and Pt–Sn–Ce/C were obtained by the relationship:

$$X_{sn} = \left(\frac{a - a_0}{a_s - a_0} \right) X_s \qquad (1)$$

where a_s and X_S are, respectively, the lattice parameter (0.4002 nm) and the Sn atomic fraction (0.25) in Pt$_3$Sn/C (ETEK) and a_0 represents the lattice parameter of Pt/C (ETEK) (0.3916) [19]. According to Eq. (1), the degree of alloying in Pt–Sn/C is lower than that in Pt–Sn–Ce/C (Table 2). Presence of a third non-alloyed component generally decreases the degree of alloying of the base binary alloy [19,24,25]. However, in our case, the presence of Ce increased the degree of alloying of Sn with Pt. More information on particle size and dispersion of the nanoparticles on carbon was obtained from TEM analysis. Fig. 3 shows the typical TEM images of Pt–Sn/C and Pt–Sn–Ce/C along with the particle size distribution histograms. The mean particle sizes of Pt–Sn/C and Pt–Sn–Ce/C are, respectively, 2.4 (5) and 2.0 (8) nm, which were estimated by averaging the diameter of 100 different nanoparticles from the TEM images (Table 2). The d_{TEM} values are higher than the d_{XRD} values, probably because the d_{TEM} may include some aggregated particles.

Fig. 4 compares the CO$_{ad}$ stripping voltammogram of the Pt–Sn/C and Pt–Sn–Ce/C catalysts. CO$_{ad}$ oxidation occurs over a wide potential domain with multiple peaks in the voltammograms

of both Pt–Sn/C and Pt–Sn–Ce/C. The onset potential for Pt–Sn/C is 0.25 V and that for Pt–Sn–Ce/C is 0.15 V. The lower onset potential of Pt–Sn–Ce/C is indicative of better CO$_{ad}$ oxidation through bifunctional mechanism. The initial peak a for Pt–Sn–Ce/C is well developed compared to the corresponding peak for Pt–Sn/C (Fig. 4). Similarly, multiple peaks b and c around 0.7 V are comparatively more resolved and developed in the case of Pt–Sn–Ce/C, but the corresponding peaks of Pt–Sn/C are highly overlapped and moved toward anodic direction.

Polyol method of reducing metal precursors is best suited for Pt–Sn based catalysts. The reducing ability of ethylene glycol is proportional to the temperature and by controlling the rate of heating, the degree of alloying can be controlled since Pt precursor salt is readily reduced at lower temperature than the Sn counterpart. PtSn nanoparticles prepared by a similar polyol reduction method in a single step yielded the surface composition of the catalyst similar to the nominal composition with a mean particle size of about 2.7 nm [26]. Pt$_{75}$Sn$_{25}$ catalyst prepared by formic acid reduction method [21] yielded nanoparticles with surface composition similar to the nominal composition. However, the mean particle size obtained by TEM analysis was about 4.7 nm. In the case of borohydride reduction method combined with a freeze-drying procedure [14], surface and bulk compositions of a series of Pt–Sn catalysts differed significantly especially for higher Sn contents. The mean particle sizes of the nanoparticles in the above case ranged 2.4–4.3 nm. Pt$_3$Sn nanoparticles with controlled sizes in the range of 3.0–6.5 nm were prepared by a novel synthesis method [15] and the average metal compositions were similar to the stoichiometric ratio. As can be seen in the XRD analysis, the degree of alloying of Sn is also influenced by the presence of Ce even though both Pt–Sn–Ce/C and Pt–Sn/C were prepared following an identical procedure. It can be noted that platinum–tin catalysts with optimal alloying and content of oxide phases of tin are desirable for high MOR activity and stability compared to unalloyed or completely alloyed catalysts. Generally, the XPS responsive surface states of Sn in platinum–tin catalysts are oxidic, independent of the Sn content in the as-prepared catalysts [13,14]. This is true in the case of Pt–Sn/C as Sn 3d spectrum shows no surface metallic Sn (Fig. 1e). However, Fig. 1b reveals the presence of surface metallic Sn in Pt–Sn–Ce/C. Addition of Ce also influences the particle size and the distribution of the nanoparticles. Both d_{XRD} and d_{TEM} reveal smaller Pt–Sn–Ce particles compared to Pt–Sn. A similar influence on particle size by the addition of a small amount of a third metal was also observed in the Pt–Sn–Ru ternary catalyst [19]. The predominant effect of Ce addition is seen in the CO$_{ad}$ stripping voltammogram (Fig. 4). CO$_{ad}$ oxidation may be promoted both by alloying and oxide phases of Sn [16,21] as well as the Ce oxide phase in Pt–Sn–Ce/C. Several features of CO$_{ad}$ oxidation on Pt–Sn/C (like onset potential) are enhanced and intensified on Pt–Sn–Ce/C due to the presence of ceria through an enhanced bifunctional mechanism.

3.2. Mechanism of methanol oxidation

Fig. 5 shows the voltammetric forward scans comparing the MOR activities of the Pt–Sn–Ce/C and Pt–Sn/C catalysts. The catalytic activity of Pt–Sn–Ce/C is higher than that of Pt–Sn/C as revealed by both the current and the peak potential values. At

Table 2
XRD and TEM characterization of Pt–Sn–Ce/C and Pt–Sn/C catalysts.

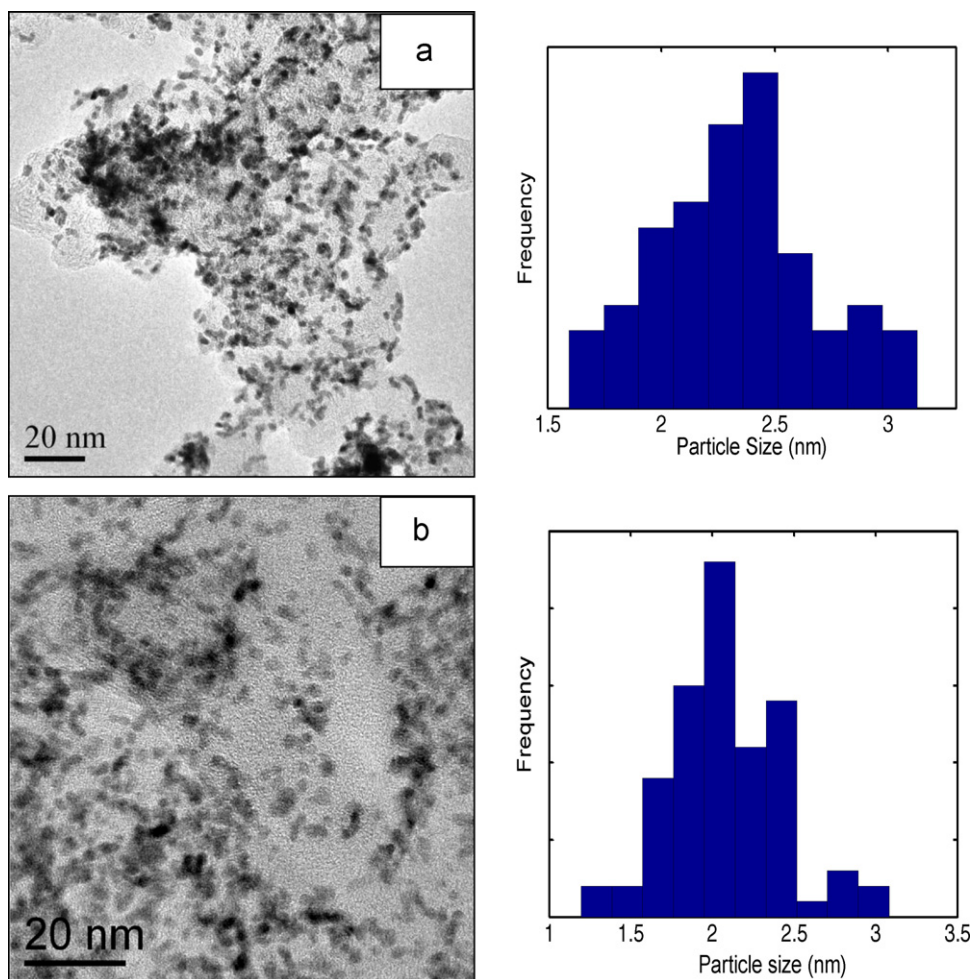| Electrocatalyst	(2 2 0) position (°)	Lattice parameter, a (nm)	Sn atomic fraction, X_{Sn}	Crystallite size, d_{XRD} (nm)	Particle size, d_{TEM} (nm)
Pt–Sn/C	66.98 (13)	0.3949 (6)	0.09	2.29	2.4 (5)
Pt–Sn–Ce/C	66.35 (18)	0.3983 (7)	0.19	1.68	2.0 (8)
Pt/C (ETEK)	67.65 (12)	0.3915 (3)	0	–	–

Fig. 3. TEM images of (a) Pt–Sn/C and (b) Pt–Sn–Ce/C with particle size distribution histograms.

0.5 V, the methanol oxidation current of Pt–Sn/C is about 55% that of Pt–Sn–Ce/C and the peak potential of Pt–Sn/C is higher than that of Pt–Sn–Ce/C by 40 mV. Various surface reactions that control the voltammetric current can be better understood by derivative voltammograms [27] that have more voltammetric features than normal voltammograms. Fig. 6 delineates the first derivative of the normal voltammograms of Fig. 5. The derivative voltammogram represents the rate of change of voltammetric current i with respect to electrode potential E (di/dE). At low potentials, dissociative adsorption of methanol occurs and with subsequent removal of hydrogen atoms from methanol, the most active surface sites of Pt are covered with adsorbed carbon monoxide (represented by point
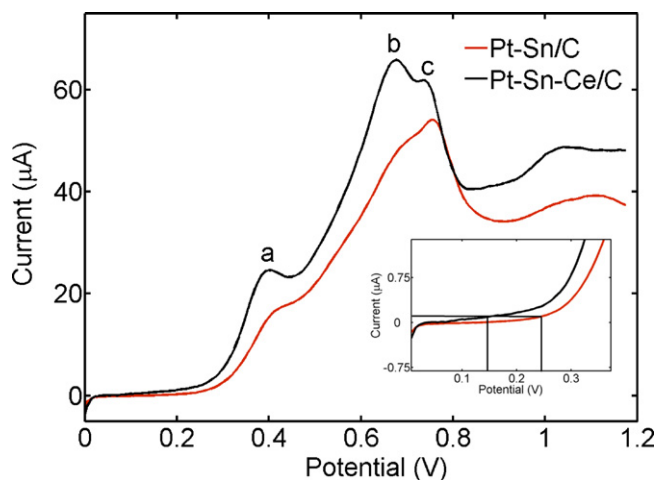
Fig. 4. CO_{ad} stripping voltammograms of Pt–Sn–Ce/C and Pt–Sn/C in 0.5 M H_2SO_4, with the inset showing an expanded region near onset potential. Scan rate = 20 mV/s.
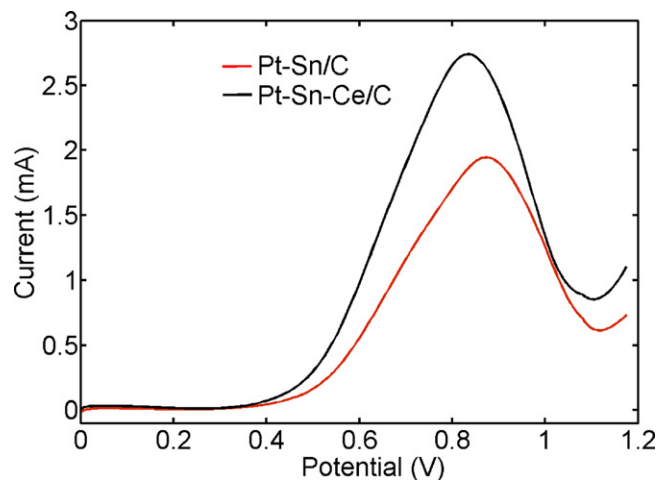

Fig. 5. Anodic scans of linear sweep voltammograms of MOR at Pt–Sn–Ce/C and Pt–Sn/C in 0.5 M H_2SO_4 + 1 M methanol. Scan rate = 50 mV/s.
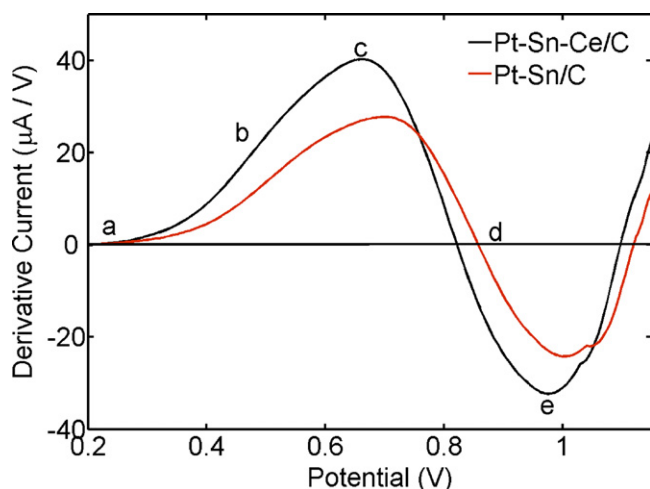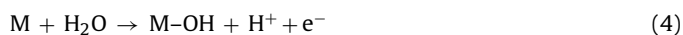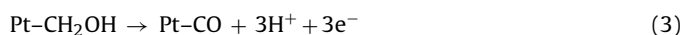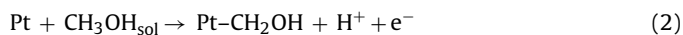
Fig. 6. Anodic scans of derivative voltammograms of MOR at Pt–Sn–Ce/C and Pt–Sn/C in 0.5 M H_2SO_4 + 1 M methanol. Scan rate = 50 mV/s.

a in Fig. 6). Methanol dehydrogenation is the rate-determining step at lower potentials (reactions (2) and (3)):

$$Pt + CH_3OH_{sol} \rightarrow Pt–CH_2OH + H^+ + e^- \qquad (2)$$

$$Pt–CH_2OH \rightarrow Pt–CO + 3H^+ + 3e^- \qquad (3)$$

$$M + H_2O \rightarrow M–OH + H^+ + e^- \qquad (4)$$

$$M–OH + Pt–CO \rightarrow CO_2 + Pt + M + H^+ + e^- \qquad (5)$$

With an increase in potential, CO_{ad} is oxidized to CO_2, freeing more sites to reactions (2) and (3). The di/dE value increases from point a to b and the oxidation of CO_{ad} to CO_2 becomes the rate determining step. The species that oxidizes CO_{ad} (e.g., OH) is generated by the secondary metals M added to Pt (reactions (4) and (5)). It can be noted that at these potentials, Pt is unable to produce OH species, so a lower onset potential is observed in Pt–M catalysts compared to Pt. Further increase in the potential results in the generation of OH on Pt sites as well, which tends to block methanol adsorption and its subsequent oxidation. The above process is indicated by decreasing di/dE value from point c. Even though voltammetric current continues to increase at this potential (Fig. 5), the rate of increase (di/dE) falls as indicated in the derivative voltammogram. The oxidative removal of OH_{ad} may be thought of as the rate-determining step at this stage. At point d, di/dE reaches zero at which point the voltammetric current reaches a maximum and starts decreasing (Fig. 5). The di/dE value becomes negative after point d since the beneficial effect of OH is now inimical as Pt sites are strongly adsorbed to OH species blocking methanol adsorption from the bulk solution. The derivative voltammogram of Pt–Sn/C is shifted toward anodic direction at points a, b, c, d, and e in comparison to the respective positions in the derivative voltammogram of Pt–Sn–Ce/C, indicating the higher overpotentials required for the above reactions at Pt–Sn/C. The above features of derivative voltammograms are corroborated by EIS as depicted in Fig. 7.

EIS has been widely employed to analyze various chemical and physical processes at the electrode surface that control the activity of the catalyst [28]. The impedance behavior of Pt–Sn–Ce/C is illustrated in Fig. 7 in the complex plane plot as a function of electrode potential. At initial lower potentials, a large arc appears and the diameter of which decreases with potential. The initial slow kinetics is caused by CO_{ad} from methanol dehydrogenation that blocks further adsorption and dehydrogenation of methanol. The arc enters into the fourth quadrant at low frequency region with further increase in potential (Fig. 7a). This behavior is called pseudo-inductive, resulting from the relaxation between
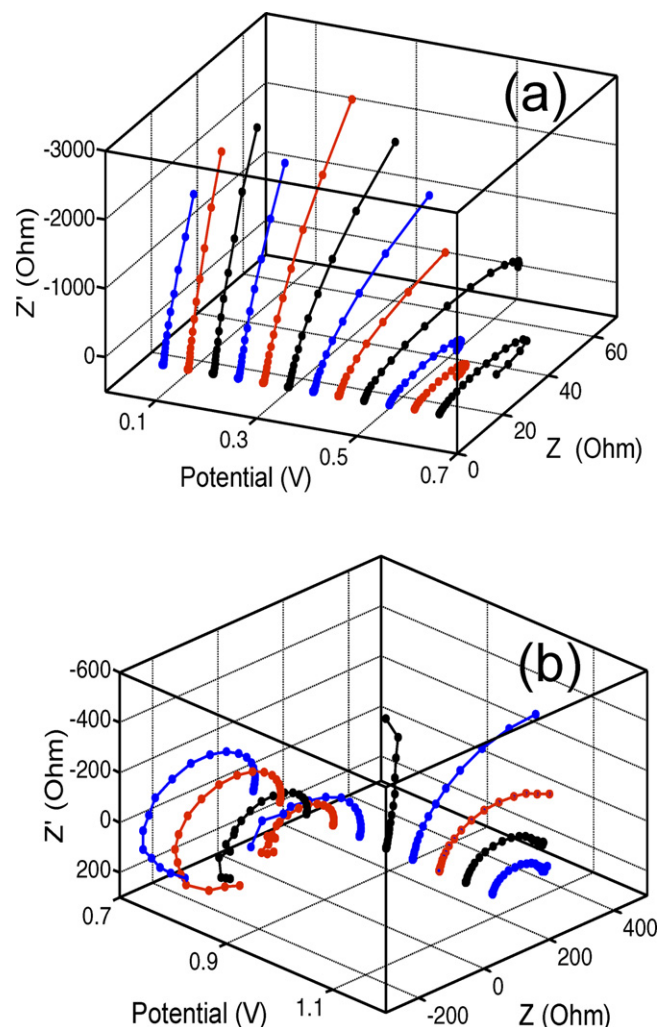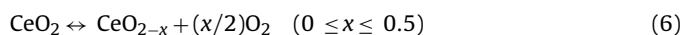

Fig. 7. Complex plane impedance plots of MOR at Pt–Sn–Ce/C as a function of electrode potential in 0.5 M H_2SO_4 + 1 M methanol.

adsorption–dehydrogenation of methanol and oxidation–adsorption of CO_{ad} [29]. The diameter of the arc both in the first and in the fourth quadrants increases with potential and flips into second and third quadrants abruptly (Fig. 7b). The rate-determining step in this potential region is the oxidative removal of CO_{ad} by OH_{ad}. It can be noted that Pt in the presence of Ce oxide exhibited pseudo-inductive behavior both in the fourth and in the third quadrants whereas the Pt electrocatalyst with SnO_2 did not show this behavior [18]. Above 0.7 V, the arc flips back in to first quadrant with its diameter decreasing with potential (Fig. 7b).

Fig. 8 compares the impedance patterns of Pt–Sn–Ce/C with those of Pt–Sn/C at 400, 650, and 800 mV. At these potentials, the reaction resistances for methanol oxidation on Pt–Sn/C is higher than those on Pt–Sn–Ce/C. Fig. 8a depicts that the rate of methanol dehydrogenation is higher on Pt–Sn–Ce/C; in other words, Pt–Sn–Ce/C has higher CO tolerance than Pt–Sn/C. Similarly, Fig. 8b and c shows that rate of oxidative removal of CO_{ad} is faster on Pt–Sn–Ce/C, which is in agreement with the results of CO_{ad} stripping voltammetry (Fig. 4). The effect of ceria on CO_{ad} oxidation can be described through bifunctional mechanism. Ceria with high oxygen carrying capacity is capable of storing and releasing oxygen with a reversible transition between the +4 and +3 oxidation states of cerium.
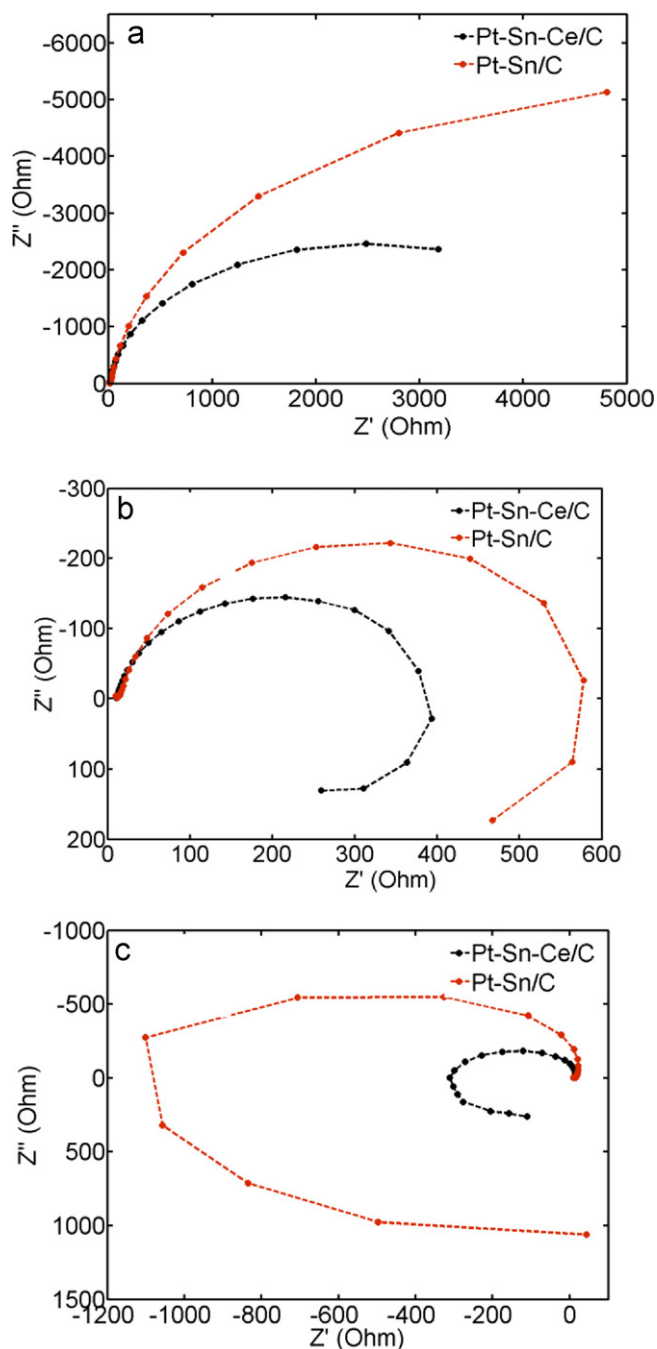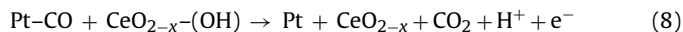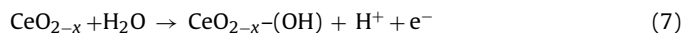
$$CeO_2 \leftrightarrow CeO_{2-x} + (x/2)O_2 \quad (0 \leq x \leq 0.5) \qquad (6)$$

Fig. 9. Variation of methanol oxidation current at 0.5 V as function of Sn/Pt ratio.

ratio. The volcano-type profile of the effect of Sn/Pt ratio on the MOR activity is known [14]. From the data in Fig. 9, the optimum Pt:Sn composition for MOR is observed as 3:1 in the presence of the minor component Ce. At lower Sn content, the oxidation of CO_{ad} may be limited due to the lack of sufficient quantity of oxygenated species at lower potentials. At higher Sn content, Pt ensembles for methanol adsorption are decreased. Therefore, at both lower and higher Sn contents, MOR is limited because of the above negative effects. However, at an optimum composition, the negative effects are minimized resulting in an enhanced MOR.

3.3. Comparison of the MOR stability and activity of Pt–Sn–Ce/C and commercial PtRu/C

Electrochemical long-term stability of anode catalyst is one of the major requirements of commercializing DMFC. In the widely used anode catalyst Pt–Ru, Ru loss is the major disadvantage of the otherwise excellent catalyst for MOR. Deactivation of Pt–Ru occurs through two major mechanisms: (i) the abnormally high dissolution of Ru and (ii) coarsening of nanoparticles during the course of fuel cell operation [17]. Even though Pt–Ru is considered to be stable at the anode potentials of DMFC, uneven potential distribution resulting in local potential spikes accelerates Ru dissolution and the problem becomes more serious in DMFC stacks. Cell reversal during fuel starvation or sudden change of load also contributes to the Ru dissolution in DMFC [31]. In this respect, platinum–tin catalyst was shown to be highly stable with negligible Sn dissolution during ADT [17]. Fig. 10 compares the normalized currents of MOR at various catalysts sampled at 0.5 V as a function of potential cycles between 0.02 and 1.2 V. Commercial Pt has the highest stability, losing only 20% of the initial activity at the end of 100th cycle. Pt–Sn–Ce/C and Pt–Sn/C retains, respectively, 60 and 55% of the initial activity at the end of ADT. Commercial PtRu, on the other hand, has lost about 75% of its initial activity. Pt–Sn–Ce/C with more alloyed tin phase is more stable than Pt–Sn/C which has more surface tin oxide phase as revealed by the XPS data. Fig. 11 compares the single cell DMFC performances of Pt–Sn–Ce/C and the commercial PtRu/C (ETEK) at 80 °C. Commercial Pt/C and Nafion 115 served as cathode and membrane in both the cells. The open circuit potentials of the cells with Pt–Sn–Ce/C and PtRu/C are, respectively, 0.68 and 0.67 V. The cell with the Pt–Sn–Ce/C anode catalyst has a maximum power density of 83 mW/cm^2 while that with the PtRu/C anode catalyst has a maximum power density of 75 mW/cm^2. The above results are consistent with the structural and electrochemical data discussed in the earlier sections.

Fig. 8. Complex plane impedance plots of MOR at Pt–Sn–Ce/C and Pt–Sn/C in 0.5 M H_2SO_4 + 1 M methanol at various electrode potentials: (a) 400 mV, (b) 650 mV, and (c) 800 mV.

Ceria promotes CO_{ad} oxidation on Pt at lower potentials as follows:

$$CeO_{2-x} + H_2O \rightarrow CeO_{2-x}-(OH) + H^+ + e^- \tag{7}$$

$$Pt-CO + CeO_{2-x}-(OH) \rightarrow Pt + CeO_{2-x} + CO_2 + H^+ + e^- \tag{8}$$

Furthermore, the oxygen vacancies in CeO_{2-x} may provide active sites for CO adsorption, thus freeing Pt sites for further reaction [30].

A preliminary study on the effect of composition on methanol oxidation current was made. Ce being a minor component, the atomic ratio of Ce/Pt was kept constant while the atomic ratio of Sn/Pt was varied from 0 to 1. Fig. 9 shows a volcano-type variation of methanol oxidation current at 0.5 V as a function of Sn/Pt
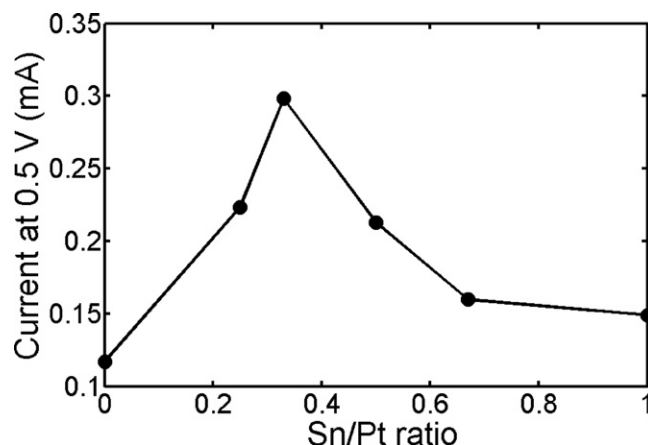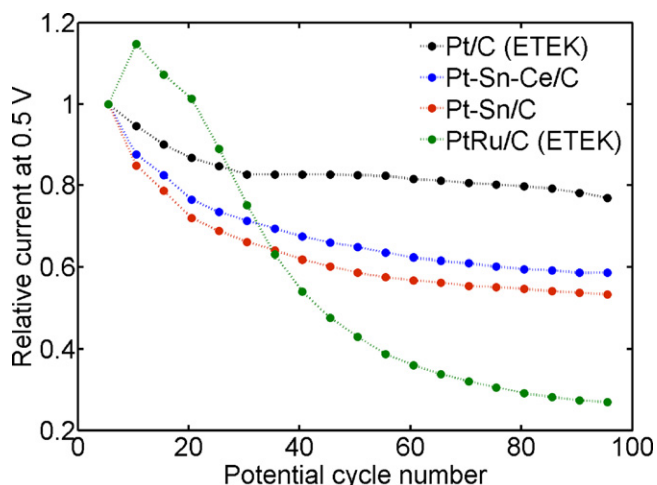
Fig. 10. Variations of the normalized currents sampled at 0.5 V for various anode catalysts as a function of potential cycles between 0.02 and 1.2 V at a scan rate of 50 mV/s in 0.5 M H_2SO_4 + 1 M methanol.
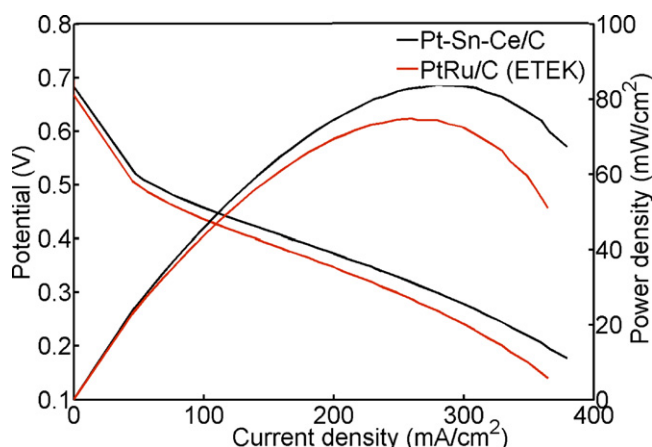

Fig. 11. Single cell performances of DMFCs consisting of Pt–Sn–Ce/C and commercial PtRu/C as anode catalysts. Pt/C and Nafion 115 served, respectively, as cathode and membrane in both the cells. Metal loading is 3 mg/cm^2 for both anode and cathode and the operating temperature is 80 °C.

4. Summary

The electrocatalytic oxidation of methanol has been compared over 40 wt.% Pt–Sn–Ce/C and Pt–Sn/C catalysts. Addition of Ce to Pt–Sn promotes MOR remarkably through (i) increasing the degree of alloying of Sn, thereby producing an optimal composition of alloyed and oxide phases; (ii) smaller particle size; and (iii) the synergetic effect of Sn and Ce oxides. Sn and Ce oxides can interact to promote oxygenated species at a lower potential, not competitively but complementarily. This synergetic effect is obvious in the CO_{ad} stripping voltammogram of Pt–Sn–Ce/C. The enhanced low potential peak of CO_{ad} stripping voltammogram (peak a in Fig. 4) shows that the bonding between CO_{ad} and Pt–Sn–Ce/C is weaker than that in Pt–Sn/C, resulting in enhanced CO tolerance. Derivative voltammetric analysis and EIS studies reveal the superior performance of Pt–Sn–Ce/C not only with respect to oxidative removal of CO_{ad}

but also with respect to the initial C—H bond dissociation. Moreover, our objective of synthesizing non-ruthenium anode catalysts with activities comparable to that of commercial Pt–Ru catalyst is demonstrated in the single cell performance of Pt–Sn–Ce/C. At the same time, stability of the catalyst is not compromised for the activity, Pt–Sn–Ce/C exhibits higher stability than Pt–Sn/C itself due to a higher degree of alloying of Sn at the catalyst surface.

References

[1] C. Lamy, A. Lima, V. LeRhun, F. Delime, C. Coutanceau, J.M. Leger, Journal of Power Sources 105 (2002) 283–296.
[2] E. Herrero, W. Chrzanowski, A. Wieckowski, Journal of Physical Chemistry 99 (1995) 10423–10424.
[3] R. Parsons, T. VanderNoot, Journal of Electroanalytical Chemistry 257 (1988) 9–45.
[4] A.S. Arico, P.L. Antonucci, E. Modica, V. Baglio, H. Kim, V. Antonucci, Electrochimica Acta 47 (2002) 3723–3732.
[5] S. Huang, S. Chang, C. Lin, C. Chen, C. Yeh, Journal of Physical Chemistry B 110 (2006) 23300–23305.
[6] T. Iwasita, Electrochimica Acta 47 (2002) 3663–3674.
[7] A.N. Haner, P.N. Ross, Journal of Physical Chemistry 95 (1991) 3740–3746.
[8] S.L. Gojkovic, T.R. Vidakovic, D.R. Durovic, Electrochimica Acta 48 (2003) 3607–3614.
[9] B.J. Hwang, L.S. Sarma, J.M. Chen, C.H. Chen, S.C. Shin, Q.R. Wang, D.G. Liu, J.F. Lee, M.T. Tang, Journal of the American Chemical Society 127 (2005) 11140–11145.
[10] B.J. Hwang, L.S. Sarma, G.R. Wang, C.H. Chen, D.G. Liu, H.S. Sheu, J.F. Lee, Chemistry: A European Journal 13 (2007) 6255–6264.
[11] C.M. Lai, J.C. Lin, K.L. Hsueh, C.P. Hwang, K.C. Tsay, L.D. Tsai, Y.M. Peng, Journal of the Electrochemical Society 155 (2008) B843–B851.
[12] Y. Sugawara, A.P. Yadav, A. Nishikata, T. Tsuru, Journal of the Electrochemical Society 155 (2008) B897–B902.
[13] A. Katayama, Journal of Physical Chemistry 84 (1980) 376–381.
[14] J.H. Kim, S.M. Choi, S.H. Nam, M.H. Seo, S.H. Choi, W.B. Kim, Applied Catalysis B 82 (2008) 89–102.
[15] Z. Liu, D. Reed, G. Kwon, M. Shamsuzzoha, D.E. Nikles, Journal of Physical Chemistry C 111 (2007) 14223–14229.
[16] F. Colmati, E. Antolini, E.R. Gonzalez, Electrochimica Acta 50 (2005) 5496–5503.
[17] E. Lee, A. Murthy, A. Manthiram, Journal of Electroanalytical Chemistry 659 (2011) 168–175.
[18] H. Yuan, D. Guo, X. Qiu, W. Zhu, L. Chen, Journal of Power Sources 188 (2009) 8–13.
[19] E. Antolini, F. Colmati, E.R. Gonzalez, Electrochemistry Communications 9 (2007) 398–404.
[20] F. Zhang, P. Wang, J. Koberstein, S. Khalid, S.-W. Chan, Surface Science 563 (2004) 74–82.
[21] F. Colmati, E. Antolini, E.R. Gonzalez, Applied Catalysis B 73 (2007) 106–115.
[22] V. Radmilovic, H.A. Gasteiger, J.P.N. Ross, Journal of Catalysis 154 (1995) 98–106.
[23] J.W. Guo, T.S. Zhao, J. Prabhuram, R. Chen, C.W. Wong, Electrochimica Acta 51 (2005) 754–763.
[24] Z. Jusys, T.J. Schmidt, L. Dubau, K. Lasch, L. Jorissen, J. Garche, R.J. Behm, Journal of Power Sources 105 (2002) 297–304.
[25] R. Venkataraman, H.R. Kunz, J.M. Fenton, Journal of the Electrochemical Society 150 (2003) A278–A284.
[26] A.O. Neto, R.R. Dias, M.M. Tusi, M. Linardi, E.V. Spinace, Journal of Power Sources 166 (2007) 87–91.
[27] S.P. Perone, T.R. Mueller, Analytical Chemistry 37 (1965) 2–9.
[28] R.E. Melnick, G.T.R. Palmore, Journal of Physical Chemistry B 105 (2001) 1012–1025.
[29] Z.-B. Wang, G.-P. Yin, Y.-Y. Shao, B.-Q. Yang, P.-F. Shi, P.-X. Feng, Journal of Power Sources 165 (2007) 9–15.
[30] Z. Sun, X. Wang, Z. Liu, H. Zhang, P. Yu, L. Mao, Langmuir 26 (2010) 12383–12389.
[31] A. Taniguchi, T. Akita, K. Yasuda, Y. Miyazaki, Journal of Power Sources 130 (2004) 42–49.